Solid state coalescence growth and electrochemical performance of plate-like Co$_3$O$_4$ mesocrystals as anode materials for lithium-ion batteries

Fei Wang*, Cancan Lu, Yifeng Qin, Congcong Liang, Mingshu Zhao, Shengchun Yang*, Zhanbo Sun, Xiaoping Song

MOE Key Laboratory for Nonequilibrium Synthesis and Modulation of Condensed Matter, School of Science, Xi'an Jiaotong University, Xi'an 710049, PR China

HIGHLIGHTS

► We describe a facile and large-scale synthesis of Co$_3$O$_4$ anode materials.
► The Co$_3$O$_4$ mesocrystals are obtained through unconventional reconstruction mechanism.
► Micrometer size Co$_3$O$_4$ mesocrystals exhibit low initial irreversible capacities.
► Superior cycling performance is obtained due to its robust mesoporous 2D structure.

GRAPHICAL ABSTRACT
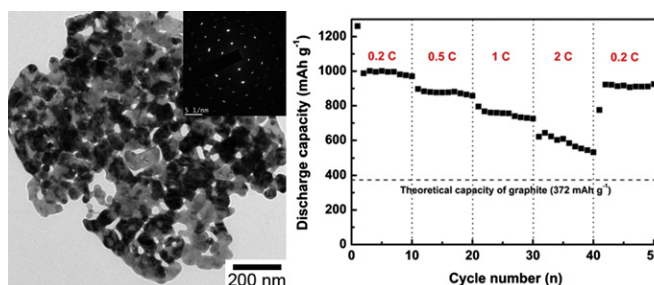
ARTICLE INFO

ABSTRACT

Co(OH)$_2$ nanosheets, which obtained from Polyvinyl Pyrrolidone (PVP) improved solution-phase synthesis, can be transformed to porous Co$_3$O$_4$ nanoplates by solid-state crystal reconstruction during heat treatment in air. Transmission electron microscopy (TEM) indicates that the transformation process and final crystal structure are strongly dependent on the temperature of heat treatment. When the temperature is increased to 500 °C, the mesoporous and single-crystal Co$_3$O$_4$ nanoplates with an average size of around 1 μm can be obtained by solid-state diffusion, coalescence and following orientational alignment. Electrochemical tests show that the lithium storage performance of porous Co$_3$O$_4$ nanoplates is associated more closely with its structural aspects than its morphology and size factors. The obtained plate-like Co$_3$O$_4$ mesocrystals exhibit low initial irreversible capacity and superior cycling performance due to its micrometer size, porous and robust single-crystal structure. Considering the improved electrochemical performance, simple and large scale synthesis, the obtained 2D Co$_3$O$_4$ mesocrystals should be suitable as anode materials for high performance lithium-ion batteries.

© 2013 Elsevier B.V. All rights reserved.

1. Introduction

"Nanoparticle" is quite an active research field not only because of the novel properties for individual nanoparticles but also owing to its new collective properties arising from nanoparticle ensembles [1,2]. Mesocrystals, which are ordered nanoparticle superstructures built up from individual nanocrystals via the alignment in common crystallographic orientation, have received rapidly increasing attention owing to their intrinsic features of rough surface, high porosity and single-crystal-like structure as well as easy processability due to their typical micrometer size [3—6]. Such property combinations make mesocrystals highly attractive in many fields, such as catalysis [7,8], sensing [9], energy storage [10—14] and other functional applications [15—19]. Nevertheless, the mechanism for mesocrystal synthesis is still poorly understood. The new physical

* Corresponding authors. Tel.: +86 29 82663034; fax: +86 29 82665995.
E-mail addresses: feiwang@mail.xjtu.edu.cn (F. Wang), ysch1209@mail.xjtu.edu.cn (S. Yang).

and chemical properties arising from the mesocrystal structure need to be revealed and their potential application as functional materials is still far from being exploited.

As an important p-type semiconductor, nanostructured Co_3O_4 has been extensively studied owing to its potential applications in gas sensors [20,21], catalysts [22,23], solar energy absorbers [24], field emission devices [25], magnetic materials [26] and super-capacitors [27,28], etc. More importantly, nanostructured Co_3O_4 is also regarded as a promising alternative anode material for rechargeable lithium ion batteries due to its high theoretical capacity of 890 mAh g^{-1} [29–42]. Nevertheless, it should be pointed out that the application of Co_3O_4 in practical lithium-ion batteries is seriously hindered by their relatively large initial irreversible loss and poor capacity retention over extended cycling [40]. The poor cyclability could originate from the large volume change during lithiation/delithiation cycles, which leads to a disintegration of the electrode material and a loss of electrical contact [43]. The large initial irreversible loss could be ascribed to side reactions such as reductive decomposition of the electrolyte and formation of a solid electrolyte interface (SEI) layer [44]. Therefore, considerable research effort has been devoted to the design and synthesis of new nanostructured cobalt oxides. It is well acceptable that the morphology, size, specific surface area and crystallinity of Co_3O_4 nanomaterials all have significant effects on the lithium-storage performance. However, the results of some methods to improve the material property are sometimes contradictory [42]. For example, the design and synthesis of nanostructured Co_3O_4 with small size and high specific surface area is beneficial for accommodating the strain associated with severe volume variations during lithiation/delithiation processes and thus effectively improve the cycling performance. While another problem of large initial irreversible loss is less considerate because the smaller size and higher specific surface area generally lead to larger initial irreversible capacities [37]. Therefore, it's significant and also a great challenge to obtain improving cyclability of Co_3O_4 in relatively large size range. Mesocrystals should be a possible structure to resolve above problems due to their typical micrometer size and high internal porosity. For example, the mesoporous single-crystal Co_3O_4 nano-needles exhibit excellent cycling performance and very low initial irreversible capacities [32]. Moreover, the crystallographically oriented mesocrystals and their special surface texture are also beneficial for electrode kinetics [40].

In this paper, we describe a facile and large-scale solution routes followed by heat treatment for synthesis of mesoporous, single-crystal Co_3O_4 nanoplates. Unlike conventional solid-state crystal reconstruction, which undergo a simple thermal recrystallization and retain the original morphology of cobalt salt precursors [32–34,38,40], in present strategy, the plate-like Co_3O_4 mesocrystals are generated by both thermal recrystallization and solid-state diffusion, coalescence as well as orientational alignment. The final morphology and size are completely different from the precursor while strongly dependent on the heat treatment temperature. The plate-like Co_3O_4 mesocrystals exhibit low initial irreversible capacity and superior cycling performance when they were used as anode material for lithium ion batteries. The improved electrochemical performance should be attributed to the unique feature of 2D Co_3O_4 mesocrystals. The results in current research should be promisingly spread to other transition metal oxides, such as CuO, Fe_2O_3/Fe_3O_4 and NiO, etc.

2. Experimental

In a typical experiment, 0.4 g PVP (Polyvinyl Pyrrolidone) and 10 mmol $CoCl_2 \cdot 6H_2O$ were dissolved in 47 mL distilled water under magnetic stirring at room temperature for 10 min. Then, 3 mL

30 wt.% ammonia solution was added quickly in above solution which turned into green immediately. Two minutes after the reaction, the green products were harvested by high-speed centrifugation and thoroughly washed by distilled water (2 times) and ethanol (2 times). The obtained green precipitates were dried in oven for 2 h at 60 °C. Finally, the dried powders were heat-treated in air for 2 h at 100–600 °C.

The structure and morphology of the products were characterized by X-ray diffraction (XRD, Bruke D8-Advance, Cu-Kα, $\lambda = 0.15406$ nm), field emission scanning electron microscope (FESEM, JEOL JSM-7100F) and transmission electron microscopy (TEM, JEOL JEM-2100). The nitrogen adsorption–desorption isotherms were measured using Micromeritics ASAP 2020M gas sorption system. BET and BJH methods were introduced to calculate surface area and pore size distribution.

Electrochemical properties of Co_3O_4 electrodes were tested using two-electrode Swagelok cells with lithium metal as the counter and reference electrodes. The working electrodes consisted of 70 wt.% active materials (Co_3O_4), 20 wt.% conductive materials (acetylene black), and 10 wt.% binder (polyvinylidene fluoride, PVDF). The electrolyte was 1 M LiPF$_6$ in a mixture of 50 vol.% ethylene carbonate (EC) and 50 vol.% diethylene carbonate (DEC). Test cells were assembled in argon filled glove box. The galvanostatical charge–discharge measurement was carried out on Arbin BT2000 battery testing system in the voltage range of 0.02 V–3.0 V (vs. Li/Li$^+$). Cyclic voltammogram was performed on Ametek VMC-4 electrochemical testing system between 3.0 V and 0 V at a scan rate of 0.5 mV s^{-1}.

3. Results and discussion

The XRD pattern of initial formed products before heat treatment shows extremely weak and broad diffraction peaks (Fig. 1a), which suggests that the crystallinity of as-prepared sample is low and the size of crystal domain is small. The diffraction peaks were found to match well with that of $Co(OH)_2$ (JCPDS No. 02-0925), indicating the following reaction occurred:

$$CoCl_2 + 2NH_3 \cdot H_2O \rightarrow Co(OH)_2 \downarrow + 2NH_4Cl \qquad (1)$$
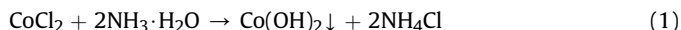
After the heat treatment for 2 h at 100 °C, the products show a similar diffraction peaks with that of as-prepared sample (Fig. 1b), indicating that $Co(OH)_2$ is stable at relatively low heating temperature. When the heat treatment temperature increased to 200 °C (Fig. 1c), the peaks of $Co(OH)_2$ disappeared, while a series of new
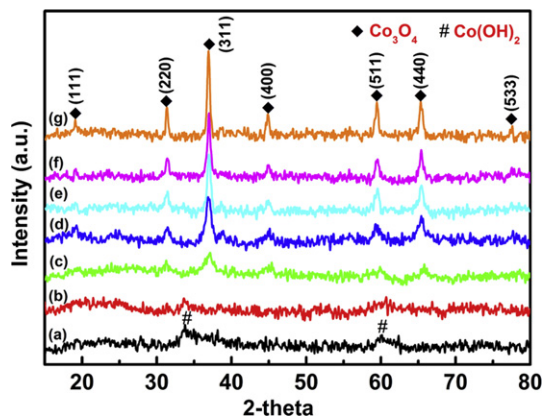

Fig. 1. XRD patterns of as-prepared sample (a) and heat treated samples at different temperatures: (b) 100 °C, (c) 200 °C, (d) 300 °C, (e) 400 °C, (f) 500 °C and (g) 600 °C.

diffraction peaks can be observed, indicating a structural transformation has occurred during the heat treatment. All diffraction peaks appearing after heat treatment at 200 °C can be indexed to the cubic Co_3O_4 (JCPDS No. 42-1467). The formation of Co_3O_4 is due to the oxidation and dehydration of $Co(OH)_2$ at high temperature, as described in Equation (2):

$$6Co(OH)_2 + O_2 \rightarrow 2Co_3O_4 + 6H_2O \qquad (2)$$
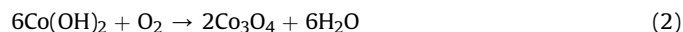
With the increase of heating temperature (Fig. 1d–g), the intensity of diffraction peaks show an obvious increasing as well as a narrowing of full width at half maximum (FWHM), indicating the crystallinity and crystallite size of the products increase along with the temperature increasing.

Fig. 2a shows the SEM image of as-prepared $Co(OH)_2$, which exhibits uniform flower-like morphology. From the inset high-resolution TEM image we can see that the flower consists of numerous ultrathin nanosheets and the thickness of single nanosheet is about 1 nm. After the $Co(OH)_2$ was annealed in air at 500 °C for 2 h, their morphology transforms to porous nanoplates with the thickness around 30 nm, as shown in Fig. 2b. In addition, the size of nanoplates grows from less than 100 nm to about 1 μm, indicating a notable growth process occurred during the heat treatment at 500 °C.

The TEM/HRTEM images with selected-area electron diffraction (SAED) and Fast Fourier transform (FFT) patterns have been used to investigate the structure and morphology transformation during the heat treatment process. Comparing with the precursor, there is no significant change in both morphology and structure after the heat treatment at 100 °C, as shown in Fig. 3a and c. The corresponding SEAD characterization shows a weak ring-like diffraction pattern (Fig. 3b), which suggests that the nanosheets are poor crystallinity, consistent with the analysis from the XRD patterns (Fig. 1a, b). When the heating temperature was further increased to 200 °C, the diffraction rings become obvious (Fig. 3e), indicating the increased crystallinity and grain size. All the diffraction rings could be assigned to the spinel-type Co_3O_4, indicating the nucleation and grain growth of Co_3O_4 from the $Co(OH)_2$ has occurred. TEM micrograph shows that the morphology of nanosheets becomes porous structure after the heat treatment at 200 °C (Fig. 3d). High-resolution TEM micrograph shows that the grain size is around 3 nm (Fig. 3f), which is in agreement with the calculated result of 2.5 nm based on the FWHM data of (311) peak by using Scherrer's formula. When the samples were annealed at the temperature of 300 °C and 400 °C, the products still keep a porous sheet-like morphology (Fig. 3g and j), while their SAED

patterns show a distinct change from the diffraction rings to discrete spots (Fig. 3h and k). It indicates that the high temperature heat treatment stimulates the grain coarsening of the samples, which can be further confirmed by HRTEM characterizations (Fig. 3i and l). As shown in Fig. 3i, the crystallite size obviously grows up to around 10 nm, and the distribution of lattice orientation is random, which can be confirmed by discrete spots in FFT pattern obtained from several selected grains (the insert in Fig. 3i). Fig. 3m is the TEM image of the sample annealing at 500 °C for 2 h, showing a porous structure with the pore size distribution from several to tens of nanometers and an obvious increase in the dimension. However, both the SAED (Fig. 3n) and FFT (the insert in Fig. 3o) spots present a regular hexagonal distribution, indicating a cubic and single-crystal characteristic. The broadening of SAED spots, especially for those of the high-index crystal planes, suggest a common orientation with a small angle lattice mismatch between the primary NP building units. The HRTEM image shown in Fig. 3o further supports this deduction, in which two crystal grains share the same crystalline orientation. These results reveal that the annealing at higher temperature evidently improves the crystallization of the products, and in addition, their porous but single crystal characteristics are well consistent with the definition of mesocrystal.

The specific surface area and BJH pore size distribution of Co_3O_4 were obtained based on the nitrogen adsorption–desorption isotherms carried out at 77 K (Fig. 4). When the $Co(OH)_2$ is heat treated at 200 °C, the structural transformation occurs and the internal pores are formed among the new phase through the oxidation and dehydration of the precursor. Moreover, due to the limited grain growth of new phase at low temperature, a high surface area can be expected at this stage. This was proven by nitrogen adsorption experiments. Fig. 4a shows that the Co_3O_4 obtained at 200 °C has high specific surface area of 118.6 $m^2\,g^{-1}$ and small pore size around 4.7 nm (peak value). Increasing the heat treatment temperature to 500 °C, the crystallite size has an obvious growth by solid-state diffusion and coalescence, which inevitably lead to the decrease of the specific surface area and increase of the pore size. As shown in Fig. 4b, the specific surface area reduces to 39.3 $m^2\,g^{-1}$ and pore size increases to around 11.6 nm (peak value). All results of nitrogen adsorption experiments are well consistent with the TEM/HRTEM characterizations.

The structure and morphology transformation processes at different heat treatment temperatures can be illustrated as Fig. 5. The precursor is polycrystalline $Co(OH)_2$ nanosheets, which can be maintained at 100 °C. When the heat treatment temperature increases to 200 °C, the morphology has a conversion from the
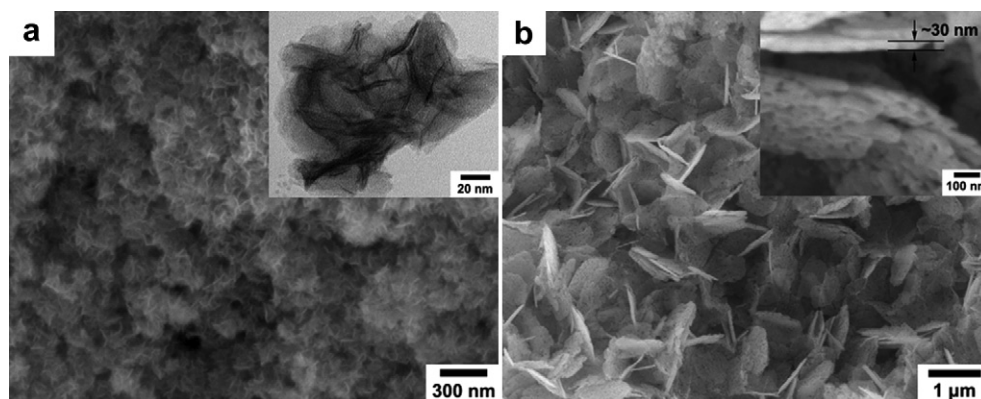

Fig. 2. SEM images of as-prepared $Co(OH)_2$ (a) and Co_3O_4 heat treated at 500 °C (b). The inset of (a) is the high-resolution TEM image of as-prepared $Co(OH)_2$, the inset of (b) is the high-resolution SEM image of Co_3O_4 heat treated at 500 °C.
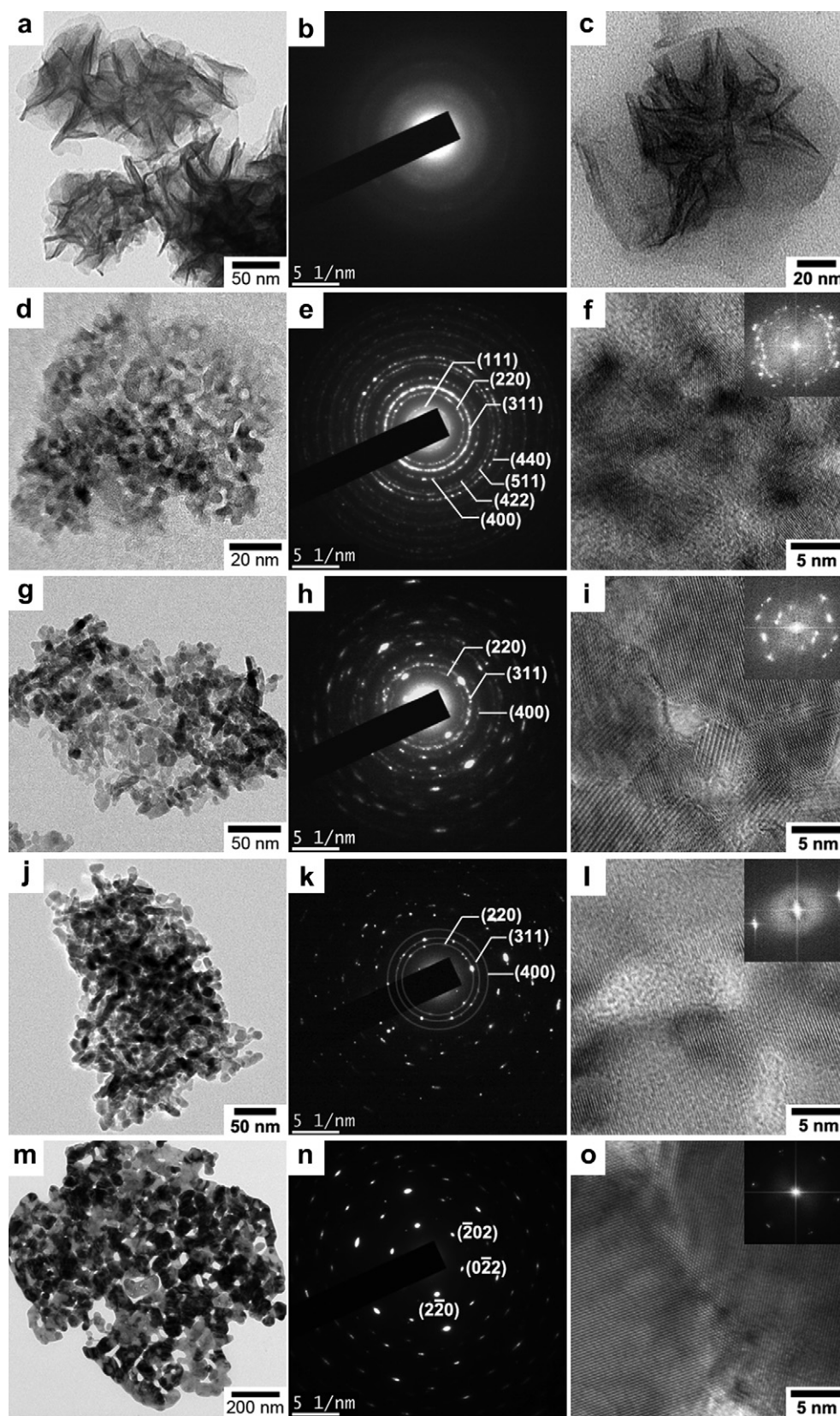
Fig. 3. The TEM images, SAED patterns and HRTEM images of heat treated samples at 100 °C (a–c), 200 °C (d–f), 300 °C (g–i), 400 °C (j–l) and 500 °C (m–o). The insets in HRTEM are the corresponding FFT patterns.
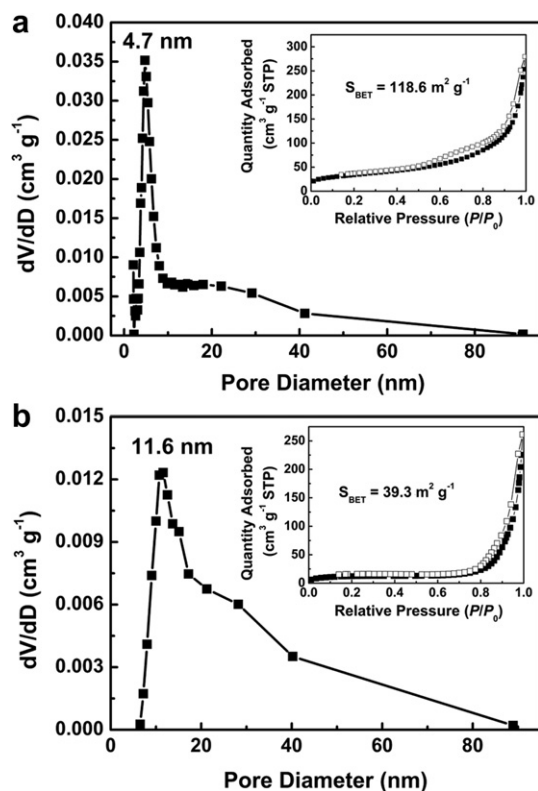
Fig. 4. Nitrogen adsorption–desorption isotherms for the Co₃O₄ heat treated at 200 °C (a) and 500 °C (b). The insets show the corresponding pore size distribution calculated by BJH method from desorption branch.

original ultrathin nanosheets to mesoporous nanosheets due to thermal recrystallization of Co₃O₄ through oxidation and dehydration of Co(OH)₂. With further increasing of the heat treatment temperature, the coalescence process begins with contact and initial fusion, followed by the orientational alignment of coalescing planes at the interface between the particles [45]. As a result, all individual nanocrystals in a single Co₃O₄ nanoplate align in common crystallographic orientation at the heat treatment

temperature of 500 °C. Simultaneously, the dimensions of Co₃O₄ nanoplates can arrive at ∼1 μm in width and ∼30 nm in thickness (Fig. 2b).

Fig. 6a illustrates the cyclic voltammograms (CV, 0.5 mV s⁻¹) of the plate-like Co₃O₄ mesocrystals heat treated at 500 °C. During the first cathodic scan, there are one shoulder around 1.0 V (indicated by arrow A in Fig. 6a), one strong peak at 0.63 V and one relatively weak peak near 0 V. The shoulder around 1.0 V should be attributed to the reduction of Co₃O₄ into CoO + L₂O, which is confirmed by the 1.1 V plateau at the first discharge curve in Fig. 6b (0.2 C, 1 C = 890 mAh g⁻¹) [43]. The peak at 0.63 V can be ascribed to the further reduction of CoO into Co + Li₂O as well as the irreversible formation of a SEI layer [29,46], corresponded to the 1.0 V voltage plateau at the first discharge cycle. The total Li-driven decomposition of Co₃O₄ can be described in Equation (3).

$$Co_3O_4 + 8Li^+ + 8e^- \leftrightarrow 4Li_2O + 3Co \qquad (3)$$
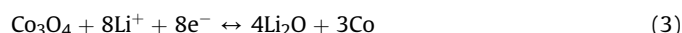
Moreover, the weak peak near 0 V, which corresponds to the continuous sloping voltage to 0.02 V at the first discharge cycle, should be associated with the reversible formation/dissolution of a gel-like film on the surface of oxide particles, which can lead to an extra reversible capacity besides the reversible reaction mechanism mentioned in Equation (3) [46,47]. Therefore, the actual reversible capacity of Co₃O₄ usually exceeds its theoretical values [32,33]. In the first anodic scan, only one peak at about 2.18 V appears, which should be ascribed to the reversible oxidation of Co to cobalt oxide. In the following cycles, the CV curves are similar, while the main cathodic peak shifts to 0.89 V due to the reduction of polarization effect after the first cycle. It is worth to mention that a very weak cathodic peak appears at about 2.2 V in stead of the shoulder around 1.0 V after the first cycle (indicated by arrow B in Fig. 6a), which can be explained by the much smaller size of the reacting grains after one cycle than in the initial oxides and the size of the clusters is not affected by extensive cycling, at least for a few cycles [43]. Correspondingly, the discharge curves after the first cycle also present a shoulder around 2.0 V. Both the cyclic voltammograms and the voltage–capacity curves exhibit highly consistent after the first cycle, which demonstrate superior cycle stability of the plate-like Co₃O₄ mesocrystals during the lithiation/delithiation processes.
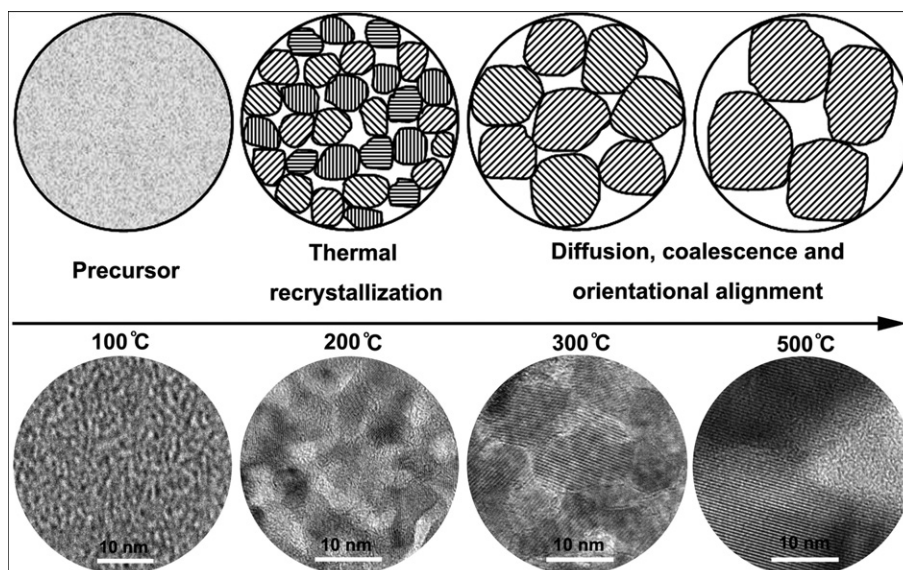

Fig. 5. Schematic illustration of structure and morphology transformation processes for the synthesis of Co₃O₄ at different temperatures.
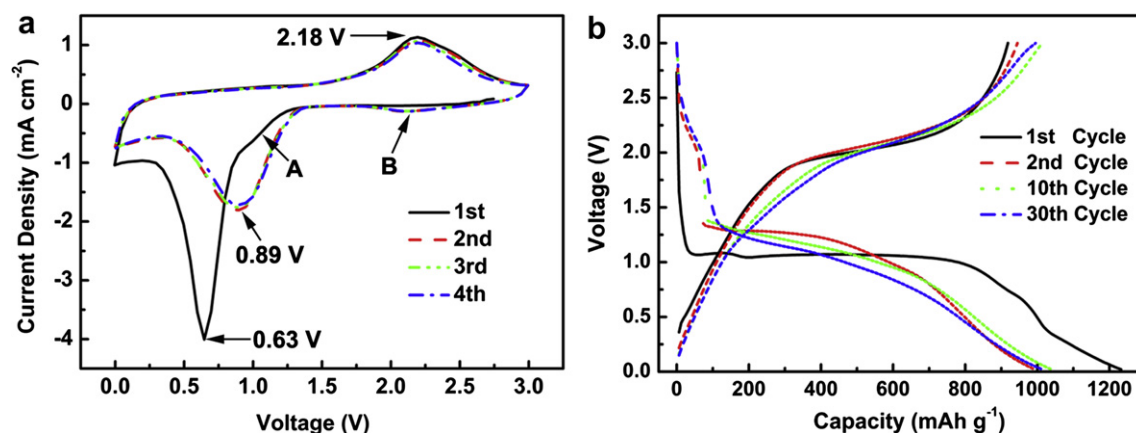
Fig. 6. Cyclic voltammograms (a) and voltage—capacity curves (b) for different cycles of the plate-like Co_3O_4 mesocrystals heat treated at 500 °C.

The coulomb efficiency and cycling performance of the plate-like Co_3O_4 mesocrystals heat treated at 500 °C are shown in Fig. 7a. The initial discharge and charge capacities are 1232 mAh g^{-1} and 918 mAh g^{-1}, respectively. The irreversible reactions are mainly attributed to decomposition of the electrolyte and formation of the SEI layer [44], which are significantly influenced by the specific surface area of anode materials. Due to the relatively large dimensions and low specific surface area of the plate-like Co_3O_4 mesocrystals, the coulomb efficiency in the first cycle is up to 74.5%. Thereafter, the coulomb efficiencies are increased gradually and stabilized around 99% after 10 cycles. Except the first cycle, no obvious capacity fade is found within 30 cycles and the discharge capacity at 30th cycle can be maintained at

1015 mAh g^{-1}. The superior cycling performance of the plate-like Co_3O_4 mesocrystals should be attributed to its mesoporous and loose structure, which is beneficial for accommodating the strain induced by the severe volume variations during Li$^+$ insertion and extraction. Fig. 7b shows the coulomb efficiency and cycling performance of the plate-like Co_3O_4 mesocrystals at 1 C. The coulomb efficiency, discharge and charge capacities of the first cycle are 71%, 1228 mAh g^{-1} and 870 mAh g^{-1}, respectively, which show a slight decreasing compared with the data at 0.2 C. The discharge capacity can be maintained at 618 mAh g^{-1} after 30 cycles. Rate capability test (Fig. 7c) also shows that the discharge capacity can be maintained at a relatively high level (>500 mAh g^{-1}) when the test current density is increased to 2 C. More importantly, the capacity

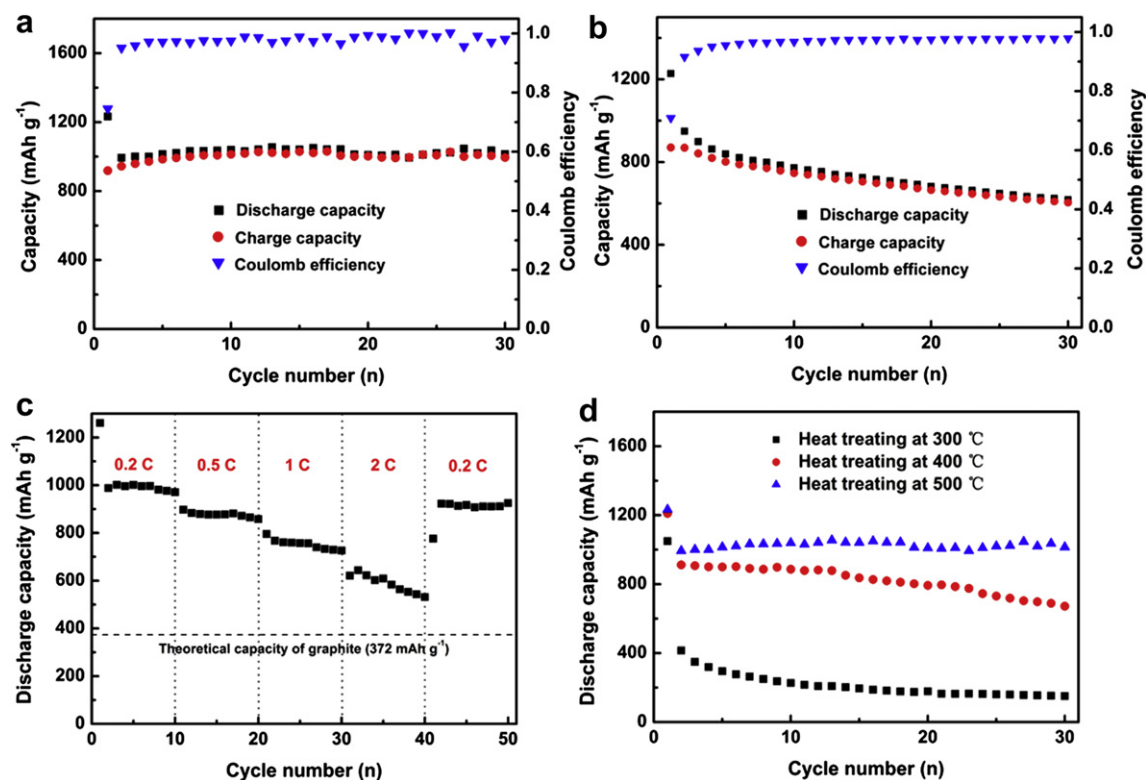**Fig. 7.** Cycling performance of the plate-like Co_3O_4 mesocrystals at 0.2 C (a) and 1 C (b); rate capability of the plate-like Co_3O_4 mesocrystals at different current densities (c); cycling performance comparison of porous Co_3O_4 nanoplates heat treated at different temperatures (d). The sample in (a)–(c) is heat treated at 500 °C, and the current density of (d) is 0.2 C.

can reincrease to the original level when the current density turns back to 0.2 C, which indicates good structural stability of the plate-like Co_3O_4 mesocrystals in fast lithiation/delithiation processes. The superior rate capability can be ascribed to the mesoporous structure and thin thickness, which can effectively shorten the Li^+ diffusion distance and thus lead to an enhanced kinetics. Moreover, the formation of crystallographically oriented mesocrystals in the cobalt oxide phases may also be propitious to the charge transfer during lithiation/delithiation processes because less crystallite boundaries present amongst the highly aligned mesocrystals [40].

Fig. 7d compares the cycling performance of porous Co_3O_4 nanoplates heat treated at 300 °C, 400 °C and 500 °C, respectively. As shown in Fig. 3, the main differences of three samples are particle size, crystallinity and crystal orientation. Considering the effect of particle size, the sample heat treated at lower temperature should have better electrochemical performance because of its smaller size and larger specific surface area. However, the results indicate that the cycling performance deteriorates with decreasing of the heat treatment temperature. Therefore, the electrochemical performance of porous Co_3O_4 nanoplates is associated more closely with its structural aspects than its morphology and size factors. More robust mesoporous structure of the Co_3O_4 mesocrystals heat treated at 500 °C should have stronger structure relationship and better structural stability during the lithiation/delithiation processes, which improves the capacity retention over prolonged discharge−charge cycles [32,33].

4. Conclusions

In summary, $Co(OH)_2$ nanosheets have been synthesized by a simple, large scale and PVP improved solution-phase route. After the heat treatment at 500 °C for 2 h, the as-prepared $Co(OH)_2$ can be transformed to the plate-like Co_3O_4 mesocrystals through thermal recrystallization combined with solid-state diffusion, coalescence and following orientational alignment. When the plate-like Co_3O_4 mesocrystals were used as anode material for lithium-ion batteries, the coulomb efficiency in the first cycle is up to 74.5% and the discharge capacity at 30th cycle can be maintained at 1015 mAh g^{-1} (0.2 C). Moreover, the obtained Co_3O_4 mesocrystals also exhibit superior rate capability. Therefore, the single-crystal 2D transition-metal oxides with robust mesoporous structure should be feasible alternative anode materials for high performance lithium-ion batteries.

Acknowledgments

References

[1] H. Goesmann, C. Feldmann, Angew. Chem. Int. Ed. 49 (2010) 1362−1395.
[2] J.F. Ye, W. Liu, J.G. Cai, S. Chen, X.W. Zhao, H.H. Zhou, L.M. Qi, J. Am. Chem. Soc. 133 (2011) 933−940.
[3] H. Cölfen, M. Antonietti, Angew. Chem. Int. Ed. 44 (2005) 5576−5591.
[4] M. Niederberge, H. Cölfen, Phys. Chem. Chem. Phys. 8 (2006) 3271−3287.
[5] L. Zhou, P. O'Brien, Small 4 (2008) 1566−1574.
[6] R.Q. Song, H. Cölfen, Adv. Mater. 22 (2010) 1301−1330.
[7] J.X. Sun, G. Chen, J. Pei, R.C. Jin, Q. Wang, X.Y. Guang, J. Mater. Chem. 22 (2012) 5609−5614.
[8] Y. Aoyama, Y. Oaki, R. Ise, H. Imai, CrystEngComm 14 (2012) 1405−1411.
[9] S. Deng, V. Tjoa, H.M. Fan, H.R. Tan, D.C. Sayle, M. Olivo, S. Mhaisalkar, J. Wei, C.H. Sow, J. Am. Chem. Soc. 134 (2012) 4905−4917.
[10] D. Wang, J. Li, X. Cao, G.S. Pang, S.H. Feng, Chem. Commun. 46 (2010) 7718−7720.
[11] J. Popovic, R. Demir-Cakan, J. Tornow, M. Morcrette, D.S. Su, R. Schlögl, M. Antoniett, M.M. Titirici, Small 7 (2011) 1127−1135.
[12] L.R. Hou, C.Z. Yuan, L. Yang, L.F. Shen, F. Zhang, X.G. Zhang, CrystEngComm 13 (2011) 6130−6135.
[13] Z.S. Hong, M.D. Wei, T.B. Lan, L.L. Jiang, G.Z. Cao, Energy Environ. Sci. 5 (2012) 5408−5413.
[14] M.W. Xu, F. Wang, B.J. Ding, X.P. Song, J.X. Fang, RSC Adv. 2 (2012) 2240−2243.
[15] Z.H. Li, A. Geβner, J.P. Richters, J. Kalden, T. Voss, C. Kübel, A. Taubert, Adv. Mater. 20 (2008) 1279−1285.
[16] M.S. Mo, S.H. Lim, Y.W. Mai, R.K. Zheng, S.P. Ringer, Adv. Mater. 20 (2008) 339−342.
[17] X.L. Wu, S.J. Xiong, Z. Liu, J. Chen, J.C. Shen, T.H. Li, P.H. Wu, P.K. Chu, Nat. Nanotechnol. 6 (2011) 103−106.
[18] S. Disch, E. Wetterskog, R.P. Hermann, G. Salazar-Alvarez, P. Busch, T. Brückel, L. Bergström, S. Kamali, Nano Lett. 11 (2011) 1651−1656.
[19] J.X. Fang, B.J. Ding, H. Gleiter, Chem. Soc. Rev. 40 (2011) 5347−5360.
[20] W.Y. Li, L.N. Xu, J. Chen, Adv. Funct. Mater. 15 (2005) 851−857.
[21] D. Patil, P. Patil, V. Subramanian, P.A. Joy, H.S. Potdar, Talanta 81 (2010) 37−43.
[22] F. Jiao, H. Frei, Angew. Chem. Int. Ed. 48 (2009) 1841−1844.
[23] C.Y. Ma, Z. Mu, J.J. Li, Y.G. Jin, J. Cheng, G.Q. Lu, Z.P. Hao, S.Z. Qiao, J. Am. Chem. Soc. 132 (2010) 2608−2613.
[24] M. Ando, K. Kadono, K. Kamada, K. Ohta, Thin Solid Films 446 (2004) 271−276.
[25] T. Yu, Y.W. Zhu, X.J. Xu, Z.X. Shen, P. Chen, C.T. Lim, J.T.L. Thong, C.H. Sow, Adv. Mater. 17 (2005) 1595−1599.
[26] M.J. Benitez, O. Petracic, E.L. Salabas, F. Radu, H. Tüysüz, F. Schüth, H. Zabel, Phys. Rev. Lett. 101 (2008) 097026.
[27] T. Zhu, J.S. Chen, X.W. Lou, J. Mater. Chem. 20 (2010) 7015−7020.
[28] F. Zhang, C.Z. Yuan, X.J. Lu, L.J. Zhang, Q. Che, X.G. Zhang, J. Power Sources 203 (2012) 250−256.
[29] P. Poizot, S. Laruelle, S. Grugeon, L. Dupont, J.-M. Tarascon, Nature 407 (2000) 496−499.
[30] K.M. Shaju, F. Jiao, A. Débart, P.G. Bruce, Phys. Chem. Chem. Phys. 9 (2007) 1837−1842.
[31] X.W. Lou, D. Deng, J.Y. Lee, J. Feng, L.A. Archer, Adv. Mater. 20 (2008) 258−262.
[32] X.W. Lou, D. Deng, J.Y. Lee, L.A. Archer, J. Mater. Chem. 18 (2008) 4397−4401.
[33] F.M. Zhang, B.Y. Geng, Y.J. Guo, Chem. Eur. J. 15 (2009) 6169−6174.
[34] L. Tian, H.L. Zou, J.X. Fu, X.F. Yang, Y. Wang, H.L. Guo, X.H. Fu, C.L. Liang, M.M. Wu, P.K. Shen, Q.M. Gao, Adv. Funct. Mater. 20 (2010) 617−623.
[35] J. Liu, H. Xia, L. Lu, D.F. Xue, J. Mater. Chem. 20 (2010) 1506−1510.
[36] J.S. Chen, T. Zhu, Q.H. Hu, J.J. Gao, F.B. Su, S.Z. Qiao, X.W. Lou, ACS Appl. Mater. Interfaces 2 (2010) 3628−3635.
[37] Y.Q. Fan, H.B. Shao, J.M. Wang, L. Liu, J.Q. Zhang, C.N. Cao, Chem. Commun. 47 (2011) 3469−3471.
[38] X.Y. Xue, S. Yuan, L.L. Xing, Z.H. Chen, B. He, Y.J. Chen, Chem. Commun. 47 (2011) 4718−4720.
[39] X. Wang, H. Guan, S.M. Chen, H.Q. Li, T.Y. Zhai, D.M. Tang, Y. Bando, D. Golberg, Chem. Commun. 47 (2011) 12280−12282.
[40] S.L. Xiong, J.S. Chen, X.W. Lou, H.C. Zeng, Adv. Funct. Mater. 22 (2012) 861−871.
[41] Y. Sun, X.Y. Feng, C.H. Chen, J. Power Sources 196 (2011) 784−787.
[42] N. Yan, L. Hu, Y. Li, Y. Wang, H. Zhong, X.Y. Hu, X.K. Kong, Q.W. Chen, J. Phys. Chem. C 116 (2012) 7227−7235.
[43] D. Larcher, G. Sudant, J.-B. Leriche, Y. Chabre, J.-M. Tarascon, J. Electrochem. Soc. 149 (2002) A234−A241.
[44] P. Poizot, S. Laruelle, S. Grugeon, L. Dupont, J.-M. Tarascon, J. Power Sources 97−98 (2001) 235−239.
[45] M. Jose-Yacaman, C. Gutierrez-Wing, M. Miki, D.Q. Yang, K.N. Piyakis, E. Sacher, J. Phys. Chem. B 109 (2005) 9703−9711.
[46] S. Laruelle, S. Grugeon, P. Poizot, M. Dolle, L. Dupont, J.-M. Tarascon, J. Electrochem. Soc. 149 (2002) A627−A634.
[47] F. Wang, W.Z. Tao, M.S. Zhao, M.W. Xu, S.C. Yang, Z.B. Sun, L.Q. Wang, X.P. Song, J. Alloys Compd. 509 (2011) 9798−9803.